PAPER

Exploring the growth and oxidation of 2D-TaS_2 on Cu(111)

IOP Publishing Nanotechnology
Nanotechnology 32 (2021) 505605 (10pp) https://doi.org/10.1088/1361-6528/ac244e

Exploring the growth and oxidation of 2D-TaS_2 on Cu(111)

Md Afjal Khan Pathan[1], Aakash Gupta[1] and Mihai E Vaida[1,2]

[1] Department of Physics, University of Central Florida, Orlando, FL 32816, United States of America
[2] Renewable Energy and Chemical Transformation Cluster, University of Central Florida, Orlando, FL 32816, United States of America

E-mail: mihai.vaida@ucf.edu

Received 5 July 2021, revised 2 September 2021
Accepted for publication 7 September 2021
Published 29 September 2021

Abstract

In this work, the growth and stability towards O_2 exposure of two dimensional (2D) TaS_2 on a Cu (111) substrate is investigated. Large area (~1 cm^2) crystalline 2D-TaS_2 films with a metallic character are prepared on a single crystal Cu(111) substrate via a multistep approach based on physical vapor deposition. Analytical techniques such as Auger electron spectroscopy, low energy electron diffraction, and photoemission spectroscopy are used to characterize the composition, crystallinity, and electronic structure of the surface. At coverages below one monolayer equivalent (ML), misoriented TaS_2 domains are formed, which are rotated up to $\pm 13^o$ relative to the Cu(111) crystallographic directions. The TaS_2 domains misorientation decreases as the film thickness approaches 1 ML, at which the crystallographic directions of TaS_2 and Cu(111) are aligned. The TaS_2 film is found to grow epitaxially on Cu(111). As revealed by low energy electron diffraction in conjunction with an atomic model simulation, the (3 × 3) unit cells of TaS_2 match the (4 × 4) supercell of Cu(111). Furthermore, the exposure of TaS_2 to O_2, does not lead to the formation of a robust tantalum oxide film, only minor amounts of stable oxides being detected on the surface. Instead, the exposure of TaS_2 films to O_2 leads predominantly to a reduction of the film thickness, evidenced by a decrease in the content of both Ta and S atoms of the film. This is attributed to the formation of oxide species that are unstable and mainly desorb from the surface below room temperature. Temperature programmed desorption spectroscopy confirms the formation of SO_2, which desorbs from the surface between 100 and 500 K. These results provide new insights into the oxidative degradation of 2D-TaS_2 on Cu(111).

Supplementary material for this article is available online

Keywords: 2D, TaS_2, transition metal dichalcogenides, oxidative degradation

(Some figures may appear in colour only in the online journal)

Introduction

After the discovery of grapheme [1], graphene-like materials, especially 2D transition metal dichalcogenides (TMDs), have been extensively studied for their unique thickness-dependent electronic and optical properties, as well as large surface to volume ratio [2]. Due to their tunable properties, these materials are excellent candidates for a wide variety of applications such as electronic and optoelectronic devices [3], photodetectors [4], chemical and gas sensors [5], catalysis [6], electrocatalysis [7], and photocatalysis [8]. Recently, studies of 2D materials have been extended to medical applications [9], wearable technology [10], energy storage applications [11], and artificial intelligence [12].

2D-TMDs can be divided into two groups based on their electronic properties: semiconducting and metallic [13–16]. Metallic TMDs have drawn attention for their unique exotic properties, such as charge density wave (CDW), superconductivity, magnetism, Mott insulating phase, metal-insulator phase transition [16–21]. Exploring 2D Weyl semimetals, phase engineering for making topological quantum devices are some of the most recent exciting research areas of metallic TMDs

[22–24]. In particular, 2D-TaS_2 has been recently studied for its rich physical properties that lead to CDW and transitions among different phases such as metallic, Mott insulating, and superconducting [25–33]. Depending on the atomic structure and orientation, 2D-TaS_2 has three crystal phases, trigonal prismatic H, octahedral T, and rhombohedral R phases. Different stacking sequences categorizes TaS_2 into 1T, 2H, 3R, 4H, etc, structures where the number in front of the phase nomenclature represents the number of stacked layers [34, 35]. The most common polymorphs of TaS_2 are 1T and 2H, both having a metallic character [16]. The possibility of engineering the electronic and structural phases as well as controlling their transition by tuning parameters such as temperature, dopants, and pressure, enriches the potential application of TaS_2 in electronic and optoelectronic devices [36–39], superconductivity [17, 31], and catalysis [40, 41]. However, the applications of TaS_2 are restricted due to the limitations in growth of uniform large-area crystalline films and the stability of this material. Several studies focused on synthesis of TaS_2 have been reported so far. Various techniques such as exfoliation [26, 36], chemical vapor deposition (CVD) [28, 41], chemical vapor transport (CVT) [42–44], arc discharge (AD) [45], powder vapor (PV) [46], and physical vapor deposition (PVD) [47] have been used for TaS_2 synthesis. The growth of TaS_2 via some of the approaches mentioned above have drawbacks. For instance, TaS_2 synthesis via exfoliation is low yield and not well controlled, which could lead to films with nonreproducible sizes and thicknesses. Therefore, it is difficult to synthesize large area single layer films via exfoliation. CVD, CVT, AD, and PV, on the other hand, are more controlled and time-efficient processes to grow 2D materials than exfoliation. However, some of these techniques do not lead automatically to large area crystalline, single layer materials. The PVD method, on the other hand, is a scalable process that allows the synthesis of 2D-TaS_2 over large areas (>1 cm^2) on various substrates. As PVD can be carried out in ultrahigh vacuum (UHV) setups, the films grown employing this method could have the highest possible purity.

Regardless of the synthesis method, a major drawback of TaS_2 is its rapid degradation when exposed to air or oxygen, as reported in literature. Luican-Mayer *et al* reported degradation of the surface of 1T-TaS_2 film after exposure to air for more than 30 min [48]. Yu *et al* correlated the deterioration of TaS_2 with changes in the contrast of optical microscopy images recorded from these films after exposure to air for different time intervals [26]. Several other studies reported the presence of oxides in TaS_2 nanoplatelets [49], nanoflakes [46, 50], and nanosheets [51] after exposure to air. Despite of the available evidences presented in literature demonstrating the ambient oxidative degradation of TaS_2, no detailed experimental investigations have been performed to understand the exact oxidation mechanism. Only theoretical studies have provided insights into the oxidation mechanism of TaS_2 [52, 53].

In this work, a multistep approach based on PVD is employed to synthesize large area crystalline 2D-TaS_2 films on Cu(111) under UHV condition. The TaS_2 surface composition, morphology, and electronic structure, are studied using various surface analytical techniques. Moreover, new insights into the TaS_2 degradation after O_2 exposure are provided.

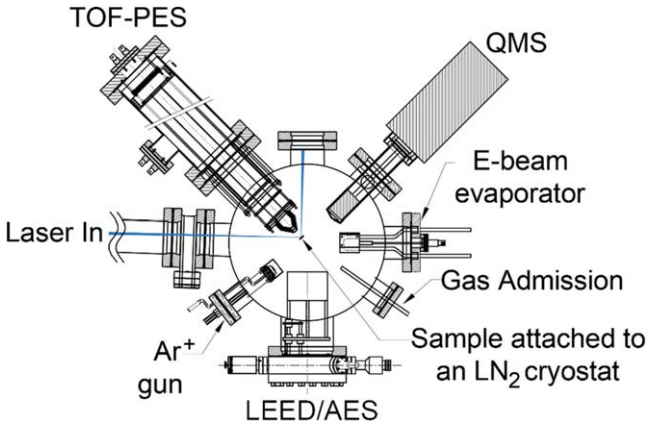

Figure 1. Schematic representation of the UHV surface science chamber employed for the preparation and characterization of the TaS_2 films.

Experimental setup

All experiments presented in this work were performed in a UHV surface science chamber, with a base pressure of $<2 \times 10^{-10}$ Torr, which is schematically represented in figure 1. The UHV chamber contains various tools for surface preparation and characterization. An Ar-ion sputtering gun is used for surface cleaning, while an electron beam evaporator is used for Ta evaporation and synthesis of 2D-TaS_2. Gases such as H_2S (99.50% purity) and O_2 (99.999% purity) are introduced in the UHV chamber through specialized inlets and used for TaS_2 synthesis and to study the stability of TaS_2 after O_2 exposure. Surface characterization tools such as low energy electron diffraction (LEED) and Auger electron spectroscopy (AES) are employed to investigate the surface crystallinity and composition, respectively. A time-of-flight photoelectron spectrometer (TOF-PES) in conjunction with femtosecond (fs) extreme ultraviolet (XUV) laser pulses generated via high order harmonic generation in rare gases are used to investigate the electronic structure of the surface. The experimental setup also contains a quadrupole mass spectrometer (QMS) that is used for residual gas analysis and temperature-programmed desorption (TPD) measurements.

A Cu(111) single crystal employed as a substrate for the TaS_2 films is attached to a liquid nitrogen cryostat, and it is mounted in the center of the UHV chamber. The surface sample-cryostat assembly can be translated vertically and horizontally as well as rotated 360° by a mechanical manipulator. The mechanical manipulator allows for a precise position of the sample in front of all preparation and characterization tools.

Synthesis and characterization of 2D-TaS_2 on Cu(111)

2D-TaS_2 is synthesized on Cu(111) via a multistep procedure based on PVD, which is schematically represented in figure 2.

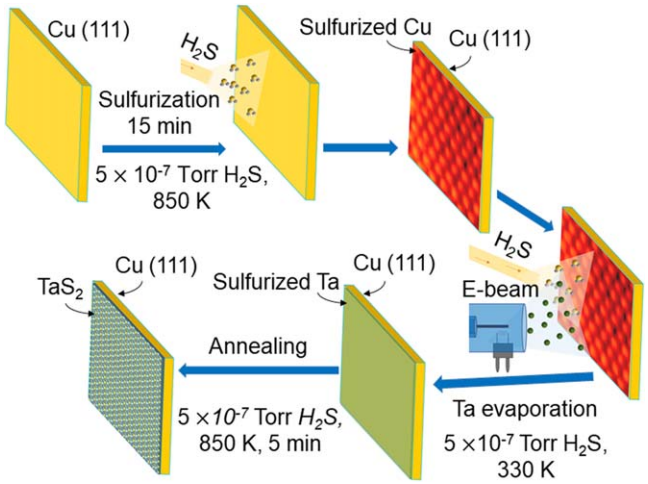

Figure 2. Schematic illustration of the multistep procedure employed to synthesize 2D-TaS_2 on Cu(111).

Before the TaS_2 preparation, the Cu(111) substrate is cleaned via subsequent cycles of Ar-ion sputtering (0.6 KV, 3 μA) for 30 min followed by flash heating at 850 K. After each cycle of sputtering and annealing, Auger electron spectra and LEED images are recorded to investigate the cleanliness and crystallinity of the substrate. The sputtering-annealing cycles are performed until no carbon, oxygen, sulfur, or any other contaminants are detected by AES.

In the first step of TaS_2 preparation, the clean Cu(111) surface is sulfurized for 15 min in a H_2S atmosphere of 5×10^{-7} Torr at 850 K, which leads to the formation of a sulfurized Cu surface. In the second step, Ta is evaporated on the sulfurized Cu surface in an H_2S atmosphere of 5×10^{-7} Torr. During the Ta evaporation, the surface temperature is maintained at 330 K. In the last preparation step, the surface is annealed at 850 K for 5 min in 5×10^{-7} Torr of H_2S.

Figure 3(a) displays AES spectra recorded from a clean Cu(111) surface, a sulfurized Cu(111) surface, and 1.1 ML sulfurized tantalum film grown on Cu(111). The Auger spectrum recorded from the clean Cu(111) substrate shows only a single peak centered at 62 eV corresponding to the MVV Auger transition of Cu (Cu_{MVV}) [54]. No peak at 273 eV corresponding to the Auger transition of carbon (C_{KLL}) [55] is detected, which indicates that the substrate is clean. The annealing of Cu(111) at 850 K in H_2S atmosphere leads to a decrease of the Cu_{MVV} peak intensity and the appearance of a new peak at 150 eV corresponding to the LMM Auger transition of sulfur (S_{LMM}) [55]. The S_{LMM} peak intensity does not increase if the H_2S partial pressure is increased above 5×10^{-7} Torr or if the exposure time is longer than 15 min, indicating that a saturated sulfurized copper layer is formed. After Ta evaporation on the sulfurized Cu, a further decrease of the Cu_{MVV} peak intensity, an increase of the S_{LMM} peak intensity, and the appearance of a new peak at 177 eV that corresponds to Ta_{NNN} Auger transition [55] are observed. These changes indicate the formation of a sulfurized tantalum layer on Cu(111), which corresponds to TaS_2, as demonstrated below.

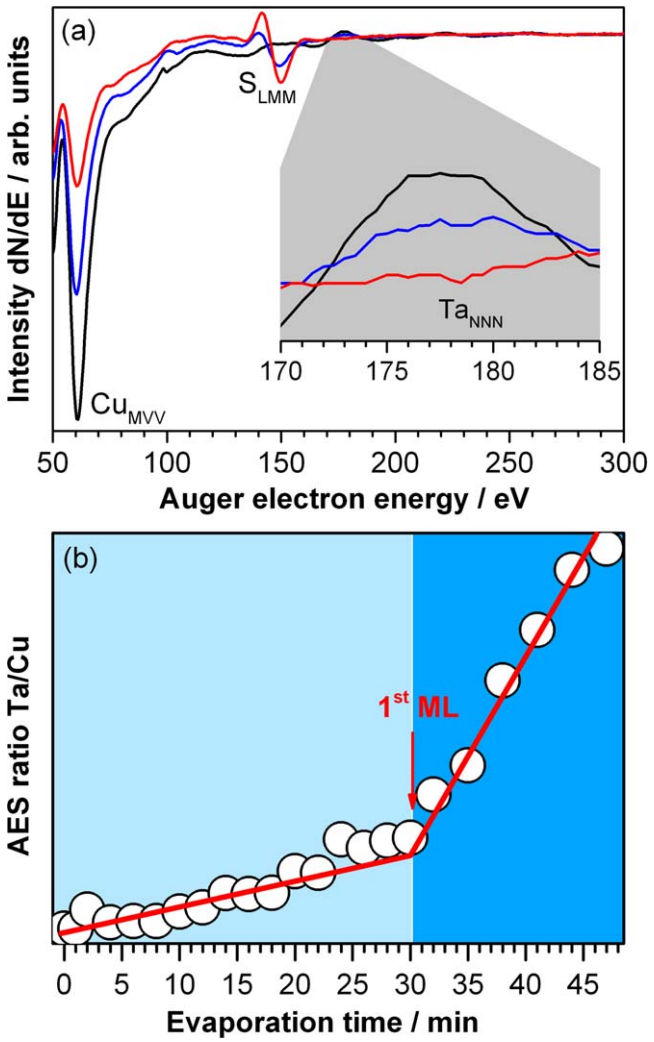

Figure 3. (a) Auger electron spectra recorded from a clean Cu(111) substrate (black curve), a sulfurized Cu(111) surface (blue curve), and a 1.1 ML TaS_2 film grown on Cu(111) (red curve). The inset displays a zoom in the 170–185 eV spectral region. (b) Auger electron intensity ratio of Ta_{NNN} to Cu_{MVV} transitions as a function of Ta evaporation time on a sulfurized Cu(111) in H_2S atmosphere. The open circles are the measured data, while the solid red lines represent linear fits to the measured data. The vertical dashed line indicates the change in the slope of the linear fit, which corresponds to the completion of the first TaS_2 layer.

AES is also employed to calibrate the Ta e-beam evaporator and determine the TaS_2 growth rate, which is subsequently used to control the thickness of the TaS_2 films. Figure 3(b) displays the ratio of intensities of Ta_{NNN} and Cu_{MVV} Auger peaks as a function of the Ta evaporation time for multiple preparations in which Ta is evaporated in H_2S atmosphere on the sulfurized Cu(111) substrate. A gradual increase of the Ta evaporation leads to a linear increase of the Ta_{NNN}/Cu_{MVV} ratio intensity until an evaporation time of 30 min. As the Ta evaporation time is increased beyond 30 min, the Ta_{NNN}/Cu_{MVV} ratio still grows linearly as a function of evaporation time, but with a higher slope. The change in slope is attributed to a change in the coefficient of attenuation of the substrate Auger signal due to the completion of the first monolayer of adsorbate [56]. Therefore, the

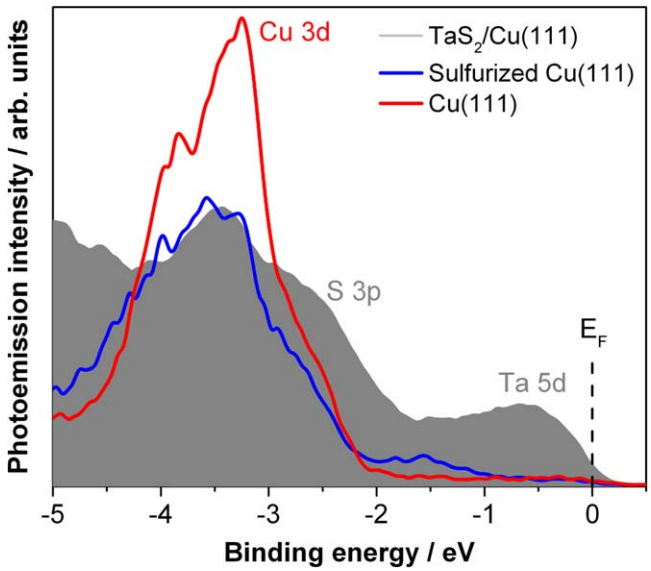

Figure 4. (a) Photoemission spectra recorded from the clean Cu(111) substrate (red curve), sulfurized Cu (blue curve) and 1.1 ML TaS_2 grown on the Cu(111) surface (shaded gray curve). The vertical dash line at 0 eV indicates the Fermi level. The photoemission spectra are recorded using XUV photons with an energy of 26.35 eV.

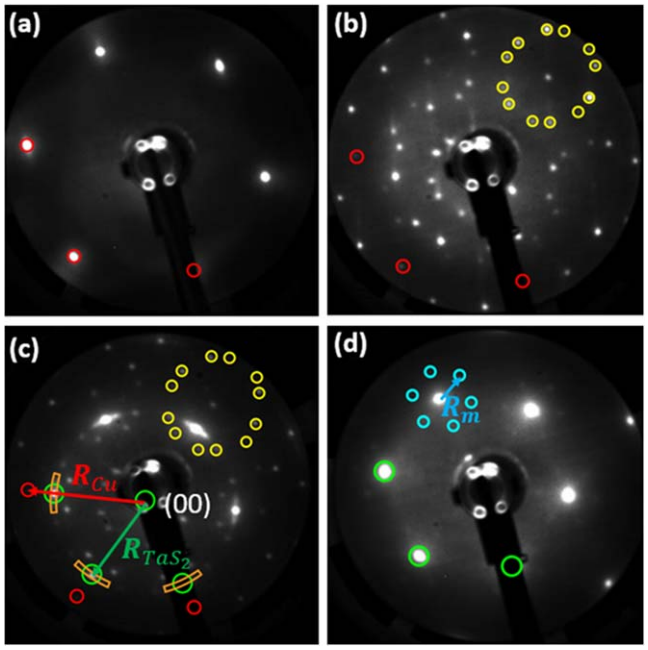

Figure 5. lEED images of (a) Cu(111), (b) sulfurized Cu(111), (c) 0.4 ML TaS_2/Cu(111), and (d) 1.1 ML TaS_2 on Cu(111). The LEED images are recorded with an electron beam energy of 79 eV. The red, yellow, and green circles mark the diffraction spots originating from Cu(111), sulfurized Cu(111), and TaS_2, respectively. The blue circles mark the diffraction spots of a Moiré pattern formed due to the epitaxial growth of TaS_2 on Cu(111). The red and green arrows in (c) indicate the distance between zero-order diffraction spot (00) and diffraction spots of Cu(111) and TaS_2, respectively. The cyan arrow in (d) indicates the distance between a TaS_2 diffraction spot and one of the Moiré spots, representing the reciprocal lattice vector of the Moiré structure.

change in slope in figure 3(b) at 30 min evaporation time corresponds to the completion of the first TaS_2 layer on the sulfurized Cu(111) surface. The rate of TaS_2 growth determined from the calibration is 0.033 ML min^{-1}.

Photoemission spectroscopy employing fs-XUV laser pulse is used to study the electronic structure of the TaS_2 film. Figure 4 displays static photoemission spectra recorded from the bare Cu(111) substrate, sulfurized Cu, and 1.1 ML TaS_2 film grown on Cu(111). The spectra are obtained using fs laser pulses with a photon energy of 26.35 eV and a bandwidth of 0.68 eV full width at half maximum (FWHM), i.e. the 17^{th} harmonic of a Ti:Sapphire laser.

All three spectra in figure 4 are displayed in the binding energy region from 0.5 to −5 eV (higher negative value corresponds to higher binding energy), where the binding energy is referenced to the Fermi level ($E_F = 0$ eV). The photoemission spectrum of Cu(111) displays occupied electronic states at E_F and a peak between −2 and −4.5 eV with a maximum at a binding energy of −3.25 eV, attributed to Cu 3d states. This spectrum resembles the features previously observed in photoemission investigations of the Cu valence band using synchrotron [57, 58] and Al Kα radiation [59].

The main effect observed after the sulfurization of the Cu(111) surface consists in a reduction of the intensity as well as an increase of the FWHM of the Cu 3d peak. Furthermore, an increase in the photoemission intensity just below −1 eV is also observed and attributed to the appearance of S 3p states. After preparation of 1.1 ML TaS_2, an increased density of states just below E_F is observed, indicating the formation of a TaS_2 film that has a metallic character, which is characteristic for both 1T and 2H phases of TaS_2. Moreover, a peak at −0.6 eV and a broadening of the photoemission feature centered at −3.25 eV through a distinct shoulder between −2 and −3 eV are also observed. The photoemission peak at −0.60 eV is attributed to the Ta 5d states, while the states at binding energy greater than −2 eV, which induced the broadening of the photoemission peak at −3.25 eV are attributed to the S 3p of TaS_2. These results are in a good agreement with the previously reported photoemission spectra of TaS_2, in which the Ta 5d states are between −0 and −1 eV and the S 3p states are between −1 and −8 eV with a peak maximum at 3.5 eV [60–62]. Therefore, the broadening of the peak at −3.25 eV and the dramatic increase of occupied electronic states just below E_F, i.e. Ta 5d states, after the evaporation of Ta in H_2S atmosphere on the Cu(111) substrate are a clear indication that TaS_2 is formed on Cu(111).

To gain insights into the structure of the TaS_2, LEED investigations are performed. Figures 5(a)–(d) displays LEED patterns recorded from a clean and a sulfurized Cu(111) substrate, as well as from 0.4 ML and 1.1 ML TaS_2 grown on the Cu(111) substrate. The diffraction image recorded from the bare substrate displays a hexagonal pattern, which is typical for the 111-crystal orientation (see red circles in figure 5). After sulfurization of the Cu(111) substrate, additional diffraction spots are visible, which correspond to a $(\sqrt{7} \times \sqrt{7})$ R19° pattern (see yellow circles in figure 5). The $(\sqrt{7}\times\sqrt{7})$ R19° structure was previously observed after Cu(111) sulfurization using H_2S [63] or benzenethiol [64].

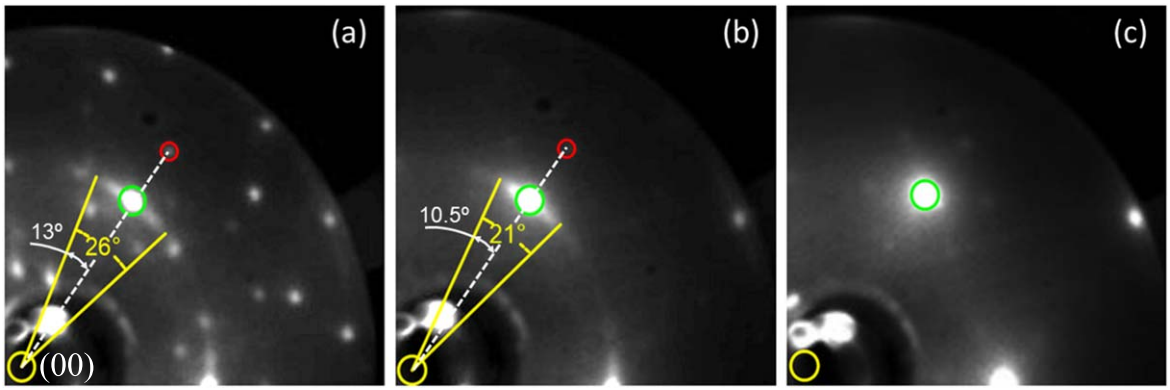

Figure 6. Thickness dependent evolution of the diffraction spots of TaS_2: (a) 0.2 ML TaS_2/Cu(111), (b) 0.4 ML TaS_2/Cu(111, and (c) 1.1 ML TaS_2/Cu(111). All images are recorded at an electron beam energy of 79 eV. For the sake of simplicity only the upper right quarter of the LEED images is shown.

After the growth of 0.4 ML TaS_2 on Cu(111), a new hexagonal diffraction pattern, centered around the (00) reflex and aligned with the diffraction pattern of Cu(111) is obtained (see green circles in figure 5). Interestingly, each new diffraction spot is composed of a sharp circular reflex (see green circles in figure 5) that overlaps an arc-shape reflex (see gold arches in figure 5(c)). The visibility of the diffraction spots from sulfurized Cu(111) clearly indicates that the surface is not fully covered by TaS_2 in the case of 0.4 ML TaS_2. The ratio of the distances from the (00) diffraction spot to a diffraction spot of Cu(111) (see red arrows in figure 5(c)) and from the (00) diffraction spot to a diffraction spot of TaS_2 (see green arrow in figure 5(c)), $R_{Cu(111)}/R_{TaS_2(1T)}$ is 1.305. This value is very close to the ratio between the lattice constant of 1T-TaS_2 ($a_{TaS_2(1T)} = 0.336$ nm) [65] and the surface lattice parameter of Cu(111), $a_{Cu(111)} = a_{Cu} \cdot \sqrt{2} = 0.255$ nm, where $a_{Cu} = 0.3597$ nm is the lattice constant of Cu [66], $a_{TaS_2(1T)}/a_{Cu(111)} = 1.317$. A similar value is also obtained if the lattice constant of 2H-TaS_2 ($a_{TaS_2(2H)} = 0.331$ nm) [67] is used $a_{TaS_2(2H)}/a_{Cu(111)} = 1.298$. This clearly demonstrates that the new diffraction spots in figure 5(c) obtained after evaporation of Ta in H_2S atmosphere are originating from TaS_2.

When 1.1 ML of TaS_2 is grown on Cu(111), a few changes are visible in the LEED pattern (see figure 5(d)): (i) the diffraction pattern of sulfurized Cu(111) vanishes indicating that the substrate is totally covered with TaS_2, which is in agreement with the AES analysis of the TaS_2 growth rate displayed in figure 3(b). (ii) The arc-shape diffraction spots disappear and the circular spots become larger in size with respect to the size of the circular diffraction spots obtained from 0.4 ML TaS_2. (iii) New smaller hexagonal diffraction patterns centered around each TaS_2 diffraction spot become visible (cyan circles in figure 5(d)), which is attributed to a Moiré pattern due to the growth of crystalline TaS_2 thin film on the Cu(111) substrate. Similar types of Moiré patterns were reported for the epitaxial growth of MoS_2 on Cu(111) [63], MoS_2 on Au(111) [68], and TaS_2 on Au(111) [47].

Note that similar AES and LEED data are recorded on various places on the sample, revealing that the composition, thickness, and crystalline structure of the obtained TaS_2 films are similar on the whole Cu(111) substrate. This indicates that the TaS_2 films obtained in this work have the same surface area as the Cu(111) surface, i.e. 1 cm^2.

Figure 6 shows the coverage dependent evolution of the TaS_2 diffraction reflexes. The angle measured between two straight lines that connect the (00) diffraction spot with the ends of the arc-shape diffraction spot (see figures 6(a) and (b)) is 26° for 0.2 ML TaS_2/Cu(111) and 21° for 0.4 ML TaS_2/Cu(111). Because the centers of the arc-shape spots are located on a straight line that connects the (00) diffraction spot with the diffraction spot of Cu(111) (dashed lines in figures 6(a) and (b)), the arc shapes in figures 6(a) and (b) have an angle ±13 deg and ±10.5 deg relative to the Cu(111) crystallographic directions. As mentioned above, the circular diffraction spot of TaS_2 grows in size as the TaS_2 amount is increased from 0.2 ML to 1.1 ML.

The arc-shape LEED reflexes observed in figures 5 and 6 are attributed to misorientation of 2D-TaS_2 domains crystallographic directions relative to the crystallographic directions of Cu(111) substrate. Misorientation of the overlayer domains with respect to the crystallographic axis of the substrate that resulted in arc-shape LEED reflexes have been reported for various 2D materials and thin films grown on single crystal metal substrates [69–73] and were attributed to the weak interaction between the substrate and overlayer.

The decrease of the angle of the arc-shape reflexes as the amount of TaS_2 is increased is attributed to a reorientation of the TaS_2 crystallographic directions with the crystallographic directions of Cu(111) substrate. This is likely due to the increased interactions between the neighboring domains, since the distance between the domains decreases as the TaS_2 coverage is increased. When the substrate is fully covered with TaS_2, all domains are oriented along crystallographic directions of Cu(111). The gradual increase in the circular spot size of TaS_2, as the TaS_2 coverage is increased from submonolayer to 1.1 ML in figure 6, is attributed to lattice mismatch that slightly grows as the TaS_2 domains reorient with the crystallographic directions of Cu(111).

Despite the large difference between the TaS_2 overlayer and substrate lattice parameters, thin films can grow epitaxially on crystalline substrates. For instance, recent

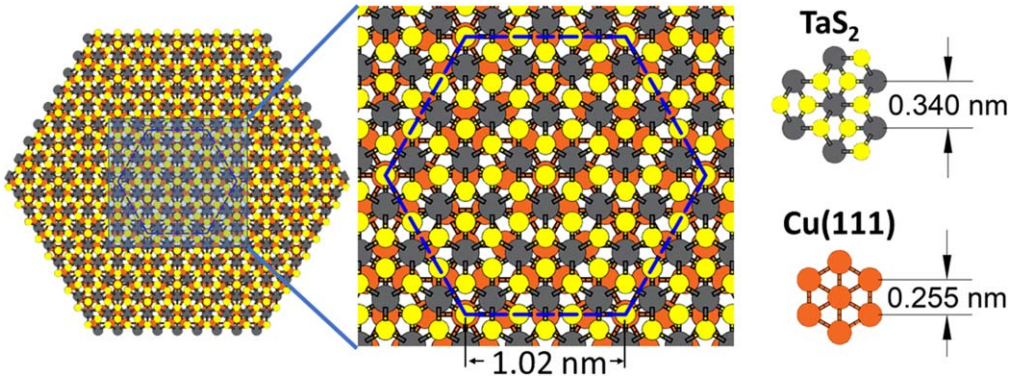

Figure 7. Ball and stick model of a single layer (3 × 3) 1T-TaS_2 on (4 × 4) Cu(111). Yellow, black, and orange circles represent S, Ta, Cu surface atoms, respectively. The blue hexagon highlights the Moiré structure.

Table 1. Calculated mismatch for ($m_1 \times m_1$) TaS_2 unit cells on a ($m_2 \times m_2$) Cu(111) supercell using the lattice parameters obtained from literature [65–67].

TaS_2 supercell and phase		Cu(111) supercell	Mismatch
(3 × 3)	1T	(4 × 4)	−1.18%
(3 × 3)	2H	(4 × 4)	−2.64%
(7 × 7)	1T	(9 × 9)	2.48%
(7 × 7)	2H	(9 × 9)	0.95%

investigations reported the epitaxial growth of MoS_2, which has a lattice constant of 0.316 nm [66], on Cu(111), which has a surface lattice parameter of 0.255 nm [63, 74]. In this case, the epitaxial growth is possible, because the size of (4 × 4) MoS_2 unit cells coincide with the size of a (5 × 5) Cu(111) surface supercell. Therefore, to better understand the epitaxial relationship between the 2D-TaS_2 and the Cu(111) substrate, an atomic model is employed. The focus of this modeling lies on reproducing the Moiré periodicity observed in the LEED investigation shown in figures 5 and 6.

The epitaxial growth of ($m_1 \times m_1$) TaS_2 unit cells on a ($m_2 \times m_2$) Cu(111) superstructure is favorable if the periodicity mismatch between the substrate and the overlayer is minimal. The mismatch in percent between the TaS_2 overlayer and the Cu(111) substrate can be calculated using the following relation $\frac{m_1 a_{TaS_2} - m_2 a_{Cu(111)}}{m_2 a_{Cu(111)}} \times 100\%$ [74]. Limiting m_1 and m_2 to 10, the smallest mismatch values are obtained for (3 × 3) TaS_2 on (4 × 4) Cu(111) and for (7 × 7) TaS_2 on (9 × 9) Cu(111), as summarized in table 1. The negative mismatch values in table 1 indicate that the ($m_1 \times m_1$) TaS_2 supercell is smaller than the ($m_2 \times m_2$) Cu(111) supercell, i.e. TaS_2 supercell needs to stretch to perfectly fit the Cu(111) supercell, while the positive mismatch values indicate the opposite, i.e. TaS_2 supercell has to compress or corrugate to perfectly fit the Cu(111) supercell.

Figure 7 displays a ball-and-stick atomic model of (3 × 3) 1T-TaS_2 on (4 × 4) Cu(111) structure. A stretch of the 1T-TaS_2 lattice constant from 0.336 nm to 0.340 nm (1.18%) leads to a perfect superposition of S and Cu atoms on a hexagonal pattern with a periodicity of 1.02 nm. The experimental Moiré periodicity is obtained by calculating the ratio of the distances from the (00) diffraction spot to a diffraction spot of Cu(111) (see R_{Cu}, red arrows in figure 5(c)) and from a TaS_2 diffraction spot to a Moiré diffraction spot (see R_m, cyan arrow in figure 5(d)). The value of $R_{Cu(111)}/R_m$, which is 4.053, should be equal to the ratio $a_m/a_{Cu(111)}$, where a_m is the real space Moiré periodicity and $a_{Cu(111)}$ is the real space surface lattice parameter of Cu(111). Accordingly, the experimental Moiré periodicity a_m is 1.034 nm $\left(a_m = \frac{R_{Cu(111)}}{R_m} \times a_{Cu(111)}\right)$. A Moiré periodicity of 1.32 nm is obtained by modeling (7 × 7) TaS_2 on (9 × 9) Cu(111) (see figure S1 (available online at stacks.iop.org/NANO/32/505605/mmedia) and discussion in the Supplementary Information).

As described above, the experimental Moiré periodicity, a_m = 1.034 nm, is very close to the Moiré periodicity of 1.02 nm obtained by modeling a (3 × 3) 1T-TaS_2 on (4 × 4) Cu(111) structure (see figure 7) and very different than the Moiré periodicity of a (7 × 7) TaS_2/(9 × 9) Cu(111) structure. Therefore, the crystalline TaS_2 structure observed in LEED (see figures 5 and 6) is attributed to an epitaxial growth of (3 × 3) TaS_2 unit cells on (4 × 4) super cells of Cu(111). Since both 1T-TaS_2 and 2H-TaS_2 have metallic characters and very close lattice constants, it is not possible to determine from LEED and XUV-PES the phase of TaS_2 on Cu(111).

Stability of TaS_2/Cu(111) towards O_2 exposure

As mentioned above, previous studies demonstrated that TaS_2 films are unstable in air, presumably due to the reaction of the film with the oxygen available in air. To obtain further insights into the stability of 2D-TaS_2 after O_2 exposure, well defined oxidation experiments are performed while the film composition, thickness, and structure are monitored.

Figure 8(a) displays Auger spectra recorded from the 3.75 ML TaS_2 film before and after exposure to 1×10^{-5} Torr O_2 for 70 min During the O_2 exposure, the surface temperature is kept at 700 K in order to enhance the expected oxidation reaction. The Auger spectrum recorded from 3.75 ML TaS_2 before oxidation displays just the S_{LMM} transition at 150 eV and Ta_{NNN} transition at 177 eV, but not the Cu_{MVV} transition at 62 eV, due to the large thickness of the film, i.e. more than 10 atomic layers, which exceeds the mean free path of the electrons originating from the substrate

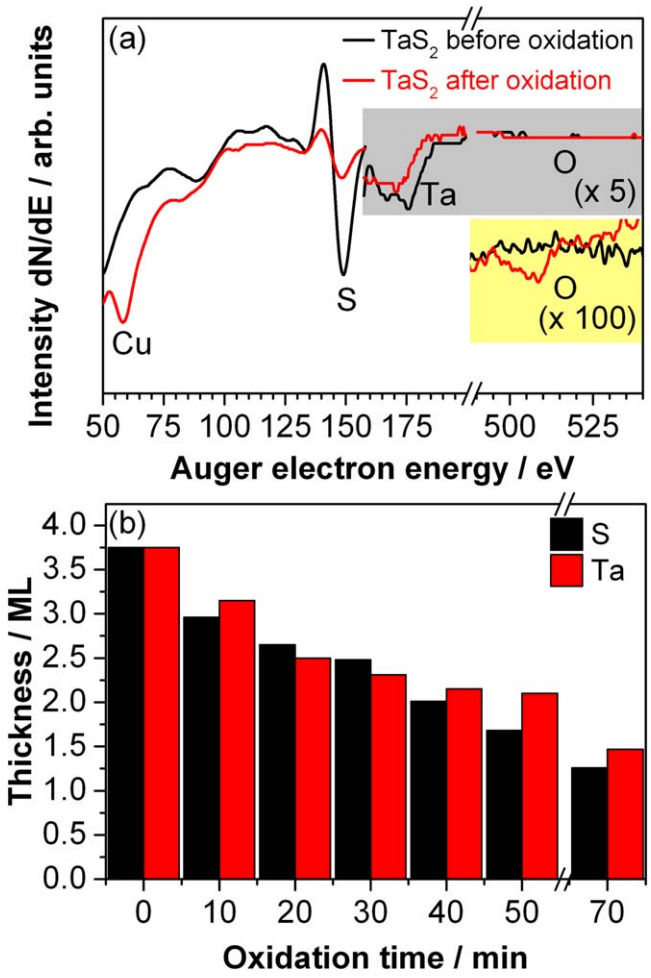

Figure 8. (a) Auger electron spectra recorded from a 3.75 ML TaS_2 film before (black curve) and after exposure to oxygen for 70 min (red curve). The gray area displays the Ta transition magnified by a factor of 5. The intensity of the spectrum in the yellow marked area is enhanced by a factor of 100 (see text for details). (b) Reduction of the TaS_2 film thickness as a function of oxygen exposure. The intensities of Ta and S peaks are converted in monolayer equivalent, to obtain insights into the thickness reduction of the TaS_2 film as a function of oxygen exposure. The O_2 partial pressure and surface temperature used to obtain the results in (a) and (b) are 1×10^{-5} Torr and 700 K, respectively.

in that energy range [75]. Surprisingly, the Auger electron spectrum recorded after exposure to oxygen shows a dramatic decrease in the intensities of both S and T peaks as well as the appearance of Cu transition, but not the appearance of predominant oxide species. Contrary, a very small intensity peak at 510 eV corresponding to the KLL Auger transition of oxygen [55] is detected only after the AES device amplification is increased by a factor 5 and the spectrum is magnified by a factor 20, i.e. a total enhancement that is 100 (5×20) higher than the portion of the spectrum below 160 eV.

The decrease in intensity of the Ta and S Auger peaks and the appearance of Cu peak after exposure to O_2 (see figure 8(a)) is attributed to the formation of oxides that are mostly unstable at 700 K, which desorb and subsequently lead to a thinning of the TaS_2 film. The very small amount of oxygen detected in the AES displayed in figure 8(a) indicates that only a small fraction of the oxides formed remain on the surface at 700 K. This can be attributed to the formation of a small amount of Ta_2O_5, which is the most stable oxide of tantalum [76]. Ta_2O_5 was previously detected in XPS when TaS_2 films were grown via CVD, in which small amounts of O_2 could be present [28] or when TaS_2 was exposed to air [77].

To obtain insights into the TaS_2 thickness reduction after exposure to oxygen, a 3.75 ML TaS_2 film has been synthesized and exposed to successively increasing doses of O_2, while the thickness of the film was monitored. Figure 8(b) displays the intensity of the Ta and S Auger peaks recorded from a 3.75 ML TaS_2 film after successive cycles of exposure to O_2. For each oxidation cycle, with a duration of 10 min, the O_2 partial pressure is kept at 1×10^{-5} Torr, while the surface temperature is kept at 700 K. The intensities of Ta and S peaks in figure 8(b) are converted in monolayer equivalent of TaS_2. As can be seen in figure 8(b), a gradual decrease of the TaS_2 thickness is obtained after successive exposures of the film to oxygen.

The thickness reduction of the TaS_2 film is also confirmed by photoemission spectroscopy. A photoemission spectrum is also recorded from a 1.1 ML TaS_2 after the surface, kept at 700 K is exposed to 1×10^{-5} Torr O_2 for 10 min (see figure S2 in the Supplementary Information). The photoemission spectrum clearly displays a decreased intensity of the Ta 5d and S 3p states, supporting the results obtained by AES.

It needs to be mentioned that no notable changes are observed when a TaS_2 film is exposed to 1×10^{-5} torr O_2 for 10–20 min, while the sample is kept between 100 and 300 K. Therefore, in order to determine if the oxidation at room temperature also leads to a thinning of the TaS_2 film, a similar oxidation experiment is performed by keeping the sample temperature at 300 K. In this case, to accelerate the oxidation process, the UHV chamber is filled with about 100 Torr of O_2 for 60 min. Figure 9 displays Auger electron spectra and LEED images recorded from a 2.35 ML TaS_2 film before and after oxidation in 100 Torr of O_2 for 60 min as well as after annealing the oxidized sample at 800 K for 1 min.

The Auger electron spectrum recorded from the 2.35 ML TaS_2/Cu(111) (see figure 9) displays only the S and Ta transition peaks, but not the Cu peak due to the large thickness of the TaS_2 film. The corresponding LEED image displays the hexagonal pattern of TaS_2, however the Moiré reflexes are not observed due to the large thickness of the TaS_2 film, which hinders the detection of the diffracted electrons from the Cu(111) substrate. After exposure of the 2.35 ML TaS_2/Cu(111) to 100 Torr O_2 for 60 min at room temperature (see figure 9), the Auger peak corresponding to S significantly diminishes, the Ta transition vanishes, while the Cu peak at 62 eV reappears. Moreover, a very small peak at 510 eV corresponding to oxygen is visible only after the intensity is increased by a factor of 100, i.e. AES device

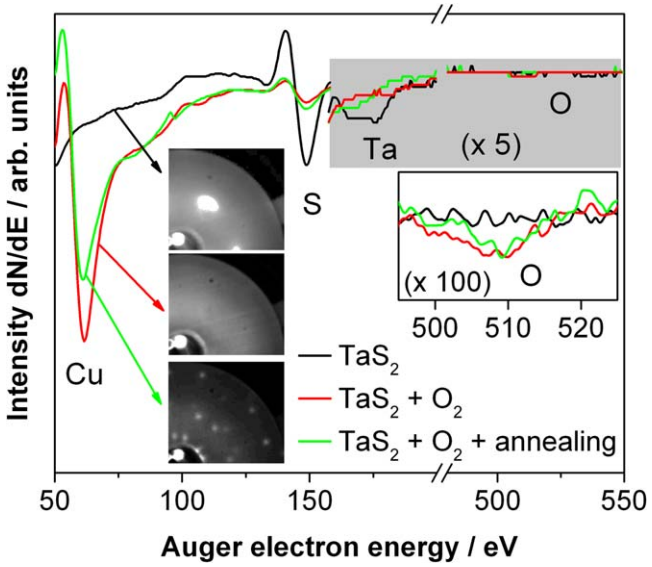

Figure 9. Auger electron spectra and LEED images recorded from a 2.35 ML TaS_2 film before (black curve) and after exposure to 100 Torr of O_2 for 60 min (red curve) as well as after annealing at 800 K the oxidized sample for 1 min (green curve). During TaS_2 exposure to O_2 the surface temperature is kept at 300 K, while during the AES and LEED analysis the sample is kept to 100 K.

amplification is increased by a factor 5 and the spectrum is magnified by a factor 20 in the 495–525 eV spectral range (see inset in figure 9). The corresponding LEED image does not display any diffraction pattern, which indicates the formation of an amorphous layer at the surface.

After annealing the oxidized TaS_2 layer for 1 min at 800 K, no dramatic changes are observed in AES. Only a narrowing of the O peak, which can be attributed to the desorption of a very small amount of oxide species from the surface during the annealing process. A diffraction pattern corresponding to $(\sqrt{7} \times \sqrt{7})$ R19° sulfurized copper is obtained after annealing the oxidized sample for 1 min at 800 K, indicating that most of the TaS_2 was oxidized and desorbed from surface, which is in agreement with the AES investigation. The structure and composition of the sulfurized copper layer does not change when it is exposed to oxygen or air at atmospheric pressure and room temperature for several hours (not shown here).

It needs to be mentioned that during the AES and LEED investigations, the sample temperature is kept at 100 K. Therefore, sample heating, due to the AES or LEED electron beam irradiation of the surface in figure 9 should be negligible and could not be responsible for the desorption of the oxides from surface. Furthermore, Auger electron spectra recorded using the same AES device and parameters from methyl halides molecules physiosorbed on oxide surfaces at 100 K did not indicated a noticeable removal of the molecules from the surface due to heating effects or electron irradiation. Consequently, most of the oxides formed during the TaS_2 exposure to 100 Torr O_2 at 300 K (see figure 9) should leave the sample during the oxidation process, but not during the AES and LEED analysis.

A recent theoretical investigation predicted that the oxidation of 1T-TaS_2 proceeds spontaneously, because there is a negligible barrier for the dissociation of physisorbed molecular oxygen at the surface of 1T-TaS_2 [53]. The physisorbed O_2 molecule is expected to dissociate within picoseconds and lead to the formation of SO_2 molecules. The calculated binding energy of the SO_2 group at the edge of 1T-TaS_2 is 1.20 eV [53].

To confirm the SO_2 formation at the surface of TaS_2 after exposure to O_2, TPD investigations have been performed. Indeed, in our experiment a very small signal at 64 amu corresponding to SO_2 is detected in TPD only if the TaS_2/Cu(111) sample is dosed with O_2 at 100 K (see figure S3 in the Supplementary Information). The thermal desorption of SO_2 extends from 100 to 500 K and has a maximum desorption at 185 K. TaO at 197 amu is not detected in the TPD experiment. Other compounds containing Ta and O could not be probed, because their mass is beyond the detection limit of the QMS, i.e. 200 amu, employed in this experiment.

The high temperature edge of the TPD spectrum obtained in this work matches the predicted binding energy of the SO_2 group at the edge of 1T-TaS_2 [53]. Moreover, the TPD investigation is in a good agreement with the results displayed in figures 8 and 9, which indicate that the exposure of TaS_2 to O_2 at a temperature equal or higher than 300 K led mostly to the formation of oxides that are unstable at room temperature and desorb. Only a small amount of oxide species obtained by the exposure of TaS_2 to O_2 are stable, which can be attributed to the formation of Ta_2O_5, as mentioned above. Therefore, we can hypostasize that in order to passivate the surface of a bulk TaS_2 material to be stable under ambient conditions, i.e. room temperature in air, multiple layers of TaS_2 need to be lost to form an oxide layer that is stable at room temperature.

Conclusions

The growth and oxidation of 2D-TaS_2 on Cu(111) is investigated using various surface science techniques. 2D-TaS_2 with an area of 1 cm^2 is grown on a Cu(111) substrate via a multistep approach based on PVD. As revealed by LEED analysis in conjunction with atomic modeling, TaS_2 grows epitaxial on Cu(111) with the (3×3) unit cells of TaS_2 matching the (4×4) supercell of Cu(111). At submonolayer coverages, a misorientation of the TaS_2 domains is detected via LEED The highest rotation angle of the TaS_2 domains is up to $\pm 13^{o}$ with respect to the Cu(111) crystallographic directions. The domains misorientation decreases by increasing the TaS_2 coverage. As the TaS_2 coverage reaches 1, the crystallographic directions of TaS_2 and Cu(111) are aligned. As revealed by various analytical techniques such as AES, LEED, PES, and TPD, exposure of TaS_2 to oxygen leads mainly to the formation of unstable oxide species that desorb from the surface at temperatures below 300 K. Only a very small amount of oxide species is found to be stable above room temperature, which are attributed to traces of Ta_2O_5 formed during the oxidation process. Consequently, the exposure to O_2 of ultrathin TaS_2 films grown on Cu(111) leads to a reduction of the films thickness.

Acknowledgments

This material is based upon work supported by the National Science Foundation under Grant No. 1943697. Aakash Gupta acknowledges financial support provided by the UCF Office of Undergraduate Research as well as by UCF through the VPR-AECR program.

Data availability statement

All data that support the findings of this study are included within the article (and any supplementary files).

ORCID iDs

Md Afjal Khan Pathan https://orcid.org/0000-0003-1094-290X
Mihai E Vaida https://orcid.org/0000-0002-2017-7757

References

[1] Novoselov K S, Geim A K, Morozov S V, Jiang D, Zhang Y, Dubonos S V, Grigorieva I V and Firsov A A 2004 Electric field effect in atomically thin carbon films *Science* **306** 666–9
[2] Tan C *et al* 2017 Recent advances in ultrathin two-dimensional nanomaterials *Chem. Rev.* **117** 6225–331
[3] Lemme M C, Li L-J, Palacios T and Schwierz F 2014 Two-dimensional materials for electronic applications *MRS Bull.* **39** 711–8
[4] Long M, Wang P, Fang H and Hu W 2018 Progress, challenges, and opportunities for 2d material based photodetectors *Adv. Funct. Mater.* **29** 1803807
[5] Anichini C, Czepa W, Pakulski D, Aliprandi A, Ciesielski A and Samori P 2018 Chemical sensing with 2D materials *Chem. Soc. Rev.* **47** 4860–908
[6] Deng D, Novoselov K S, Fu Q, Zheng N, Tian Z and Bao X 2016 Catalysis with two-dimensional materials and their heterostructures *Nat. Nanotechnol.* **11** 218–30
[7] Jin H, Guo C, Liu X, Liu J, Vasileff A, Jiao Y, Zheng Y and Qiao S Z 2018 Emerging two-dimensional nanomaterials for electrocatalysis *Chem. Rev.* **118** 6337–408
[8] Luo B, Liu G and Wang L 2016 Recent advances in 2D materials for photocatalysis *Nanoscale* **8** 6904–20
[9] Jayakumar A, Surendranath A and Pv M 2018 2D materials for next generation healthcare applications *Int. J. Pharm.* **551** 309–21
[10] Yi F, Ren H, Shan J, Sun X, Wei D and Liu Z 2018 Wearable energy sources based on 2D materials *Chem. Soc. Rev.* **47** 3152–88
[11] Kumar K S, Choudhary N, Jung Y and Thomas J 2018 Recent advances in two-dimensional nanomaterials for supercapacitor electrode applications *ACS Energy Lett.* **3** 482–95
[12] Kalita H, Krishnaprasad A, Choudhary N, Das S, Dev D, Ding Y, Tetard L, Chung H S, Jung Y and Roy T 2019 Artificial neuron using vertical MoS_2/graphene threshold switching memristors *Sci. Rep.* **9** 53
[13] Wang Q H, Kalantar-Zadeh K, Kis A, Coleman J N and Strano M S 2012 Electronics and optoelectronics of two-dimensional transition metal dichalcogenides *Nat. Nanotechnol.* **7** 699–712
[14] Mak K F and Shan J 2016 Photonics and optoelectronics of 2D semiconductor transition metal dichalcogenides *Nat. Photon.* **10** 216–26
[15] Novoselov K S, Mishchenko A, Carvalho A and Castro Neto A H 2016 2D materials and van der Waals heterostructures *Science* **353** aac9439
[16] Han G H, Duong D L, Keum D H, Yun S J and Lee Y H 2018 Van der waals metallic transition metal dichalcogenides *Chem. Rev.* **118** 6297–336
[17] Sipos B, Kusmartseva A F, Akrap A, Berger H, Forro L and Tutis E 2008 From mott state to superconductivity in 1T-TaS_2 *Nat. Mater.* **7** 960–5
[18] Porer M, Leierseder U, Menard J M, Dachraoui H, Mouchliadis L, Perakis I E, Heinzmann U, Demsar J, Rossnagel K and Huber R 2014 Non-thermal separation of electronic and structural orders in a persisting charge density wave *Nat. Mater.* **13** 857–61
[19] Xi X, Wang Z, Zhao W, Park J-H, Law K T, Berger H, Forró L, Shan J and Mak K F 2015 Ising pairing in superconducting $NbSe_2$ atomic layers *Nat. Phys.* **12** 139–43
[20] Xi X, Zhao L, Wang Z, Berger H, Forro L, Shan J and Mak K F 2015 Strongly enhanced charge-density-wave order in monolayer $NbSe_2$ *Nat. Nanotechnol.* **10** 765–9
[21] Li L J, O'Farrell E C, Loh K P, Eda G, Ozyilmaz B and Castro Neto A H 2016 Controlling many-body states by the electric-field effect in a two-dimensional material *Nature* **529** 185–9
[22] Cho S, Kim S, Kim J H, Zhao J, Seok J, Keum D H, Baik J, Choe D-H, Chang K J and Suenaga K 2015 Phase patterning for ohmic homojunction contact in $MoTe_2$ *Science* **349** 625–8
[23] Keum D H *et al* 2015 Bandgap opening in few-layered monoclinic $MoTe_2$ *Nat. Phys.* **11** 482–6
[24] Sun Y, Wu S-C, Ali M N, Felser C and Yan B 2015 Prediction of Weyl semimetal in orthorhombic $MoTe_2$ *Phys. Rev.* B **92** 161107
[25] Hellmann S *et al* 2010 Ultrafast melting of a charge-density wave in the Mott insulator 1T-TaS_2 *Phys. Rev. Lett.* **105** 187401
[26] Yu Y *et al* 2015 Gate-tunable phase transitions in thin flakes of 1T-TaS_2 *Nat. Nanotechnol.* **10** 270–6
[27] Cho D, Cheon S, Kim K S, Lee S H, Cho Y H, Cheong S W and Yeom H W 2016 Nanoscale manipulation of the Mott insulating state coupled to charge order in 1T-TaS_2 *Nat. Commun.* **7** 10453
[28] Fu W *et al* 2016 Controlled synthesis of atomically thin 1T-TaS_2 for tunable charge density wave phase transitions *Chem. Mater.* **28** 7613–8
[29] Haupt K, Eichberger M, Erasmus N, Rohwer A, Demsar J, Rossnagel K and Schwoerer H 2016 Ultrafast metamorphosis of a complex charge-density wave *Phys. Rev. Lett.* **116** 016402
[30] Ma L *et al* 2016 A metallic mosaic phase and the origin of Mott-insulating state in 1T-TaS_2 *Nat. Commun.* **7** 10956
[31] Navarro-Moratalla E *et al* 2016 Enhanced superconductivity in atomically thin TaS_2 *Nat. Commun.* **7** 11043
[32] Vogelgesang S, Storeck G, Horstmann J G, Diekmann T, Sivis M, Schramm S, Rossnagel K, Schäfer S and Ropers C 2017 Phase ordering of charge density waves traced by ultrafast low-energy electron diffraction *Nat. Phys.* **14** 184–90
[33] Wen W, Zhu Y, Dang C, Chen W and Xie L 2019 Raman spectroscopic and dynamic electrical investigation of multi-state charge-wave-density phase transitions in 1 T-TaS_2 *Nano Lett.* **19** 1805–13
[34] Wilson J A, Di Salvo F J and Mahajan S 2001 Charge-density waves and superlattices in the metallic layered transition metal dichalcogenides *Adv. Phys.* **50** 1171–248
[35] Lazar P, Martincová J and Otyepka M 2015 Structure, dynamical stability, and electronic properties of phases

inTaS$_2$from a high-level quantum mechanical calculation *Phys. Rev.* B **92** 224104

[36] Liu G, Debnath B, Pope T R, Salguero T T, Lake R K and Balandin A A 2016 A charge-density-wave oscillator based on an integrated tantalum disulfide-boron nitride-graphene device operating at room temperature *Nat. Nanotechnol.* **11** 845–50

[37] Vaskivskyi I, Mihailovic I A, Brazovskii S, Gospodaric J, Mertelj T, Svetin D, Sutar P and Mihailovic D 2016 Fast electronic resistance switching involving hidden charge density wave states *Nat. Commun.* **7** 11442

[38] Liu G, Zhang E X, Liang C D, Bloodgood M A, Salguero T T, Fleetwood D M and Balandin A A 2017 Total-ionizing-dose effects on threshold switching in $1{T}$ -TaS$_2$ charge density wave devices *IEEE Electron Device Lett.* **38** 1724–7

[39] Zhu C *et al* 2018 Light-tunable 1T-TaS$_2$ charge-density-wave oscillators *ACS Nano* **12** 11203–10

[40] Huan Y *et al* 2018 Vertical 1T-TaS$_2$ synthesis on nanoporous gold for high-performance electrocatalytic applications *Adv. Mater.* **30** e1705916

[41] Shi J *et al* 2017 Two-dimensional metallic tantalum disulfide as a hydrogen evolution catalyst *Nat. Commun.* **8** 958

[42] Enomoto H, Kawano T, Kawaguchi M, Takano Y and Sekizawa K 2004 Van der waals growth of thin Tas$_2$on layered substrates by chemical vapor transport technique *Japan J. Appl. Phys.* **43** L123–6

[43] Liu Y, Ang R, Lu W J, Song W H, Li L J and Sun Y P 2013 Superconductivity induced by Se-doping in layered charge-density-wave system 1T-TaS$_{2-x}$Se$_x$ *Appl. Phys. Lett.* **102** 192602

[44] Yoshida M, Suzuki R, Zhang Y, Nakano M and Iwasa Y 2015 Memristive phase switching in two-dimensional 1T-TaS$_2$ crystals *Sci. Adv.* **1** e1500606

[45] Raj I, Duan Y, Kigen D, Yang W, Hou L, Yang F and Li Y 2018 Catalytically enhanced thin and uniform TaS$_2$ nanosheets for hydrogen evolution reaction *Front. Mater. Sci.* **12** 239–46

[46] Zhao R, Grisafe B, Ghosh R K, Holoviak S, Wang B, Wang K, Briggs N, Haque A, Datta S and Robinson J 2018 Two-dimensional tantalum disulfide: controlling structure and properties via synthesis *2D Mater.* **5** 025001

[47] Sanders C E, Dendzik M, Ngankeu A S, Eich A, Bruix A, Bianchi M, Miwa J A, Hammer B, Khajetoorians A A and Hofmann P 2016 Crystalline and electronic structure of single-layer TaS$_2$ *Phys. Rev.* B **94** 081404

[48] Luican-Mayer A, Guest J R and Hla S-W 2015 Suppression of charge density wave phases in ultrathin 1T-TaS$_2$ arXiv:1506.04102

[49] Chick K Y, Nath M and Parkinson B A 2006 TaS$_2$ nanoplatelets produced by laser ablation *J. Mater. Res.* **21** 1243–7

[50] Chamlagain B, Cui Q, Paudel S, Cheng M M-C, Chen P-Y and Zhou Z 2017 Thermally oxidized 2D TaS$_2$ as a high-κ gate dielectric for MoS$_2$ field-effect transistors *2D Mater.* **4** 031002

[51] Wang X, Liu H, Wu J, Lin J, He W, Wang H, Shi X, Suenaga K and Xie L 2018 Chemical growth of 1T-TaS$_2$ monolayer and thin films: robust charge density wave transitions and high bolometric responsivity *Adv. Mater.* **30** 1800074

[52] Martincová J, Otyepka M and Lazar P 2020 Atomic-scale edge morphology, stability, and oxidation of single-layer 2H-TaS$_2$ *ChemPlusChem* **85** 2557–64

[53] Martincová J, Otyepka M and Lazar P 2020 Oxidation of metallic two-dimensional transition metal dichalcogenides: 1T-MoS$_2$ and 1T-TaS$_2$ *2D Mater.* **7** 045005.

[54] Hofmann S 2013 *Auger- and X-ray Photoelectron Spectroscopy in Materials Science A User-Oriented Guide* (Berlin: Springer)

[55] Vickerman J C and Gilmore I S (ed) 2009 *Surface Analysis: The Principal Techniques* Second Edition (Weinheim: Wiley-VCH)

[56] Bryant K W and Bozack M J 2005 Monolayer growth modes of Re and Nb on 4H-SiC(0001) and 4H-SiC(0001) *J. Appl. Phys.* **97** 024904

[57] Stöhr J, McFeely F R, Apai G, Wehner P S and Shirley D A 1976 Photoemission from Cu valence bands using 50–175 eV synchrotron radiation *Phys. Rev.* B **14** 4431–8

[58] Stöhr J, Apai G, Wehner P S, McFeely F R, Williams R S and Shirley D A 1976 Angle-resolved photoemission from valence bands of Cu and Au single crystals using 32–200 eV synchrotron radiation *Phys. Rev.* B **14** 5144–55

[59] Apai G, Stöhr J, Williams R S, Wehner P S, Kowalczyk S P and Shirley D A 1977 Angle-resolved photoemission from Cu single crystals using Al Kα radiation *Phys. Rev.* B **15** 584–9

[60] Clerc F *et al* 2004 Spin–orbit splitting in the valence bands of 1T-TaS$_2$ and 1T-TaSe$_2$ *J. Phys.:Condens. Matter.* **16** 3271–8

[61] Shepherd F R 1975 Photoemission studies of layer materials *PhD Thesis* Imperial College, London

[62] Eppinga R, Sawatzky G, Haas C and Van Bruggen C 1976 Photoelectron spectra of 2H-TaS$_2$ and Sn$_x$TaS$_2$ *J. Phys. C: Solid State Phys.* **9** 3371

[63] Young B T, Pathan M A K, Jiang T, Le D, Marrow N, Nguyen T, Jordan C E, Rahman T S, Popolan-Vaida D M and Vaida M E 2020 Catalytic C$_2$H$_2$ synthesis via low temperature CO hydrogenation on defect-rich 2D-MoS$_2$ and 2D-MoS$_2$ decorated with Mo clusters *J. Chem. Phys.* **152** 074706

[64] Sun D *et al* 2012 An MoS(x) structure with high affinity for adsorbate interaction angew *Chem. Int. Ed. Engl.* **51** 10284–8

[65] Spijkerman A, de Boer J L, Meetsma A, Wiegers G A and van Smaalen S 1997 X-ray crystal-structure refinement of the nearly commensurate phase of 1T-TaS$_2$ (3 + 2) dimensional superspace *Phys. Rev.* B **56** 13757–67

[66] Rumble J 2020 *CRC Handbook of Chemistry and Physics* (Boca Raton, FL: CRC Press)

[67] Meetsma A, Wiegers G A, Haange R J and De Boer J L 1990 Structure of 2H-TaS$_2$ *Acta Crystallogr.* C **46** 1598–9

[68] Bana H *et al* 2018 Epitaxial growth of single-orientation high-quality MoS$_2$ monolayers *2D Mater.* **5** 035012

[69] Varykhalov A and Rader O 2009 Graphene grown on Co(0001) films and islands: electronic structure and its precise magnetization dependence *Phys. Rev.* B **80** 035437

[70] Hattab H *et al* 2011 Growth temperature dependent graphene alignment on Ir(111) *Appl. Phys. Lett.* **98** 141903

[71] Yang B *et al* 2012 Thin silica films on Ru(0001): monolayer, bilayer and three-dimensional networks of [SiO$_4$] tetrahedra *Phys. Chem. Chem. Phys.* **14** 11344–51

[72] Jiao L *et al* 2015 Molecular-beam epitaxy of monolayer MoSe$_2$: growth characteristics and domain boundary formation *New J. Phys.* **17** 053023

[73] Usachov D Y *et al* 2018 Cobalt-assisted recrystallization and alignment of pure and doped graphene *Nanoscale* **10** 12123–32

[74] Le D, Sun D, Lu W, Bartels L and Rahman T S 2012 Single layer MoS$_2$ on the Cu(111) surface: first-principles electronic structure calculations *Phys. Rev.* B **85** 075429

[75] Seah M P and Dench W A 1979 Quantitative electron spectroscopy of surfaces *Surf. Interf. Anal.* **1** 2–11

[76] Garg S P, Krishnamurthy N, Awasthi A and Venkatraman M 1996 The O–Ta (Oxygen–Tantalum) system *J. Phase Equilib.* **17** 63–77

[77] Chamlagain B, Cui Q, Paudel S, Cheng M M-C, Chen P-Y and Zhou Z 2017 Thermally oxidized 2D TaS$_2$ as a high-κ gate dielectric for MoS$_2$ field-effect transistors *2D Mater.* **4** 031002